Supplementary Information

Ultrahigh-Sensitivity Organic Photodetectors Processed with Non-Halogenated Solvent for Self-Powered Mechano-Optoelectronic Coupled Sensing System

Baofa Lan[a]#, Xianfeng Jin[b][c]#, Zhenhua yang[d], Jia Wang[a], Wenying Zhou[a], Yingshi Guan[e], Jian Zhu[d], Zhaofeng Wang[b][c]*, Bin Kan[a]*

[a] School of Materials Science and Engineering, National Institute for Advanced Materials, Nankai University, Tianjin 300350, China.

[b] Shandong Laboratory of Advanced Materials and Green Manufacturing at Yantai, Yantai, Shandong 264006, China.

[c] State Key Laboratory of Solid Lubrication, Lanzhou Institute of Chemical Physics, Chinese Academy of Sciences, Lanzhou, Gansu 730000, China.

[d] School of Materials Science and Engineering, National Institute for Advanced Materials, Smart Sensing interdisciplinary Science Center, Nankai University, Tianjin 300350, China.

[e] Institute of Advanced Materials and School of Chemistry and Chemical Engineering, Southeast University, Nanjing 211189, China.

#These authors contributed equally to this work.

*Corresponding E-mails: kanbin04@nankai.edu.cn (B. K.); zhfwang@licp.cas.cn (Z. W.)

Contents

1. Materials

The Glass/ITO substrate, PEN/ITO substrate, and PEDOT:PSS (Baytron P VP Al 4083) were purchased from Advanced Election Technology Co., Ltd. The PM6 and L8-BO-X were purchased from Jiaxing Hyper Optoelectronics Technology Co., Ltd. The electronic transport material poly[[2,7-bis(2-ethylhexyl)-1,2,3,6,7,8-hexahydro-1,3,6,8-tetraoxobenzo[lmn][3,8] phenanthrol-ine-4,9-diyl] -2,5-thiophenedi-yl[9,9-bis[3-(dimethylamino)propyl]-9H-fluorene-2,7-di-yl]-2,5-thiophenediyl (PNDIT-F3N) were purchased from YirouPV Technology Limited. All other reagents and chemicals, including ortho-xylene (*o*-XY), methanol, deionized water, acetone, isopropanol, 1,8-diiodooctane (DIO), and silver (Ag) were directly purchased from commercial sources and used without further purification unless otherwise specified. ML phosphor ZnS:Cu was purchased from Shanghai lvmi Technology Co., Ltd.

2. Device Fabrication

ML device fabrication

The ML layer was fabricated by homogeneously mixing ZnS:Cu powders into the PDMS matrix at a weight ratio of 4:6. The PDMS was composed of base and crosslinker at a weight ratio of 10:1. The composite was placed in a vacuum chamber for 30 mins to remove air bubbles. Subsequently, the ZnS:Cu/PDMS composite was cured at 80°C for 2 h, followed by natural cooling.

OPD device fabrication

The OPDs were fabricated using a conventional structure comprising ITO/PEDOT:PSS/Active layer/PNDIT-F3N/Ag. Rigid and flexible devices were fabricated on glass and PEN substrates, respectively. For rigid devices, the ITO-coated glass was cleaned with deionized water, acetone, and isopropyl alcohol through ultrasonication for 10 min sequentially. A thin layer of PEDOT:PSS was deposited on the ITO substrate at 4000 rpm for 20 s and then annealed in air at 160°C for 15 min. For flexible devices, the PEN/ITO substrate is wiped with non-woven fabric dipped in isopropyl alcohol. A thin layer of PEDOT:PSS was deposited on the ITO substrate at 4000 rpm for 20 s and then annealed in air at 110°C for 15 min. Following this, the substrates were transferred to a glovebox filled with nitrogen. The active layer solutions

of PM6:L8-BO-X (1:1.2) were prepared by dissolving in *o*-xylene (*o*-XY) at donor concentrations of 10 mg/mL and 0.35 vol% 1,8-diiodooctane (DIO) was employed as a solvent additive. All solutions were stirred at 100°C for 3 h and then spin-coated after cooling to 80°C. The active layer was spun onto the PEDOT:PSS layer at 2000 rpm for 20 s, followed by thermal annealing at 100°C for 5 min. The thickness of active layer was controlled to be ~170 nm. After cooling, a methanol solution of PNDIT-F3N (1 mg/mL) was spin-coated on top of the active layer at 3300 rpm for 20 s. Finally, an Ag electrode with a thickness of 120 nm was evaporated under a vacuum of 1×10^{-4} Pa. The active area of the device is defined by the mask as 0.0324 cm^2.

3. Measurements and Instruments

ML device charcterization. ML signals were obtained via an optical fiber linked to a collimator (BFC-441; Zolix Instruments Co., Ltd.). Then the obtained signals were transmitted into a CCD camera (iVac-316; Edmund Optics Ltd.), which was attached to a spectrometer (Omni-λ300i; Zolix Instruments Co., Ltd.). The cyclic mechanical deformation of the ML unit is actuated by a custom-fabricated stretch-testing apparatus.

OPD device characterization. The current density-voltage (*J-V*) curve of the OPD was recorded in air using a Keithley 4200 source measurement unit and a probe station with a shielded vacuum chamber at room temperature. A QE-R solar cell spectral response measurement system was used to measure the external quantum efficiency (EQE) values of the devices.

ML-OPD system characterization. For ML-OPD system characterization, during ML linear motor drive stretching/contraction, the OPD current signal was synchronously recorded via a Keithley 2601B source measurement unit. During the application demonstration phase, during ML mechanical finger drive stretching/contraction, the OPD current signal was synchronously performed on a Keithley 4200 Source Meter Unit (SMU) at room temperature. All photographs and videos were taken with a SAMSUNG S24.

UV-visible-near infrared (UV-vis-NIR) absorption. UV-vis-NIR absorption spectra and transmission spectra were recorded on a Cary 5000 UV-vis spectrophotometer. Each film sample was spin-coated on quartz substrate.

Noise current density spectrum. Use the Keithley 4200 Source Meter Unit (SMU) to measure the I-*t* characteristic curve and directly obtain the noise current density spectrum through the built-in FFT function.

Cutoff frequency. Cutoff frequency of the devices was measured with 520 nm laser and modulated by a function generator and digital oscilloscope (Tektronix 4 series B MSO).

Response time. Response time of the devices was measured with 520 nm laser and modulated by a function generator and digital oscilloscope (Tektronix 4 series B MSO) with a fixed measurement bandwidth of 20 KHz.

4. Supporting Figures and Tables

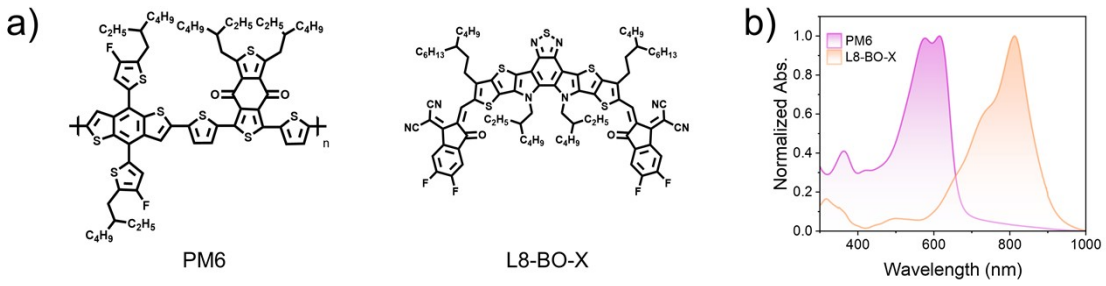

Figure S1. (a) Molecular structure of OPD active layer material where PM6 acts as a donor and L8-BO-X acts as an acceptor. (b) Normalized UV-visible-near infrared absorption spectra of PM6 and L8-BO-X.

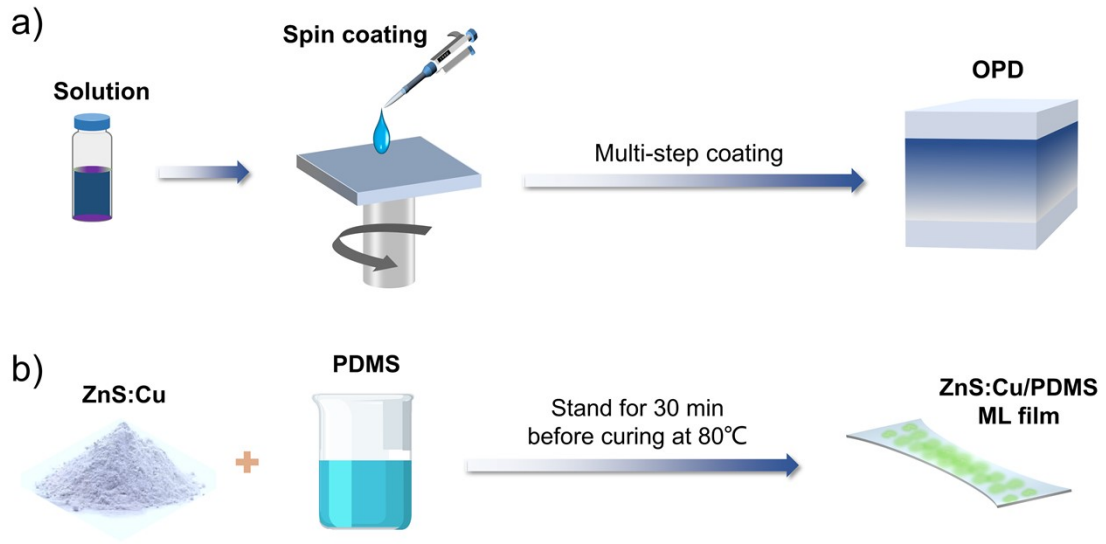

Figure S2. Device preparation schematic diagram. (a) OPD preparation process. (b) ML preparation process.

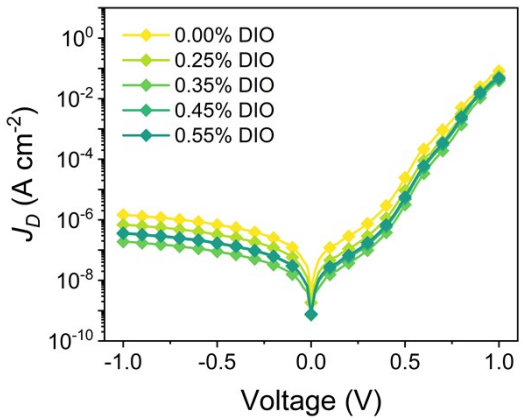

Figure S3. Additive (DIO) dosage optimization for rigid OPDs based on PM6:L8-BO-X.

Table S1. Additive (DIO) dosage optimization for rigid OPDs based on PM6:L8-BO-X.

D:A	Concentration (mg mL^{-1})	Solvent	Additive (%)	TA	Coating speed (rpm s^{-1})	J_D (A cm^{-2})
1:1.2	22	*o*-XY	0.00	100℃/5 min	2500	5.5×10^{-9}
			0.25			1.8×10^{-9}
			0.35			7.2×10^{-10}
			0.45			7.4×10^{-10}
			0.55			7.8×10^{-10}

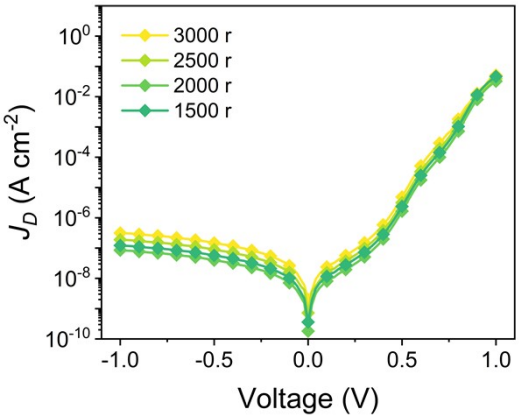

Figure S4. Optimization of BHJ thickness for rigid OPDs based on PM6:L8-BO-X.

Table S2. Optimization of BHJ thickness for rigid OPDs based on PM6:L8-BO-X.

D:A	Concentration (mg mL^{-1})	Solvent	Additive (%)	TA	Coating speed (rpm s^{-1})	J_D (A cm^{-2})
1:1.2	22	*o*-XY	0.35	100℃/5 min	3000	2.0×10^{-9}
					2500	7.2×10^{-10}
					2000	1.8×10^{-10}
					1500	3.6×10^{-10}

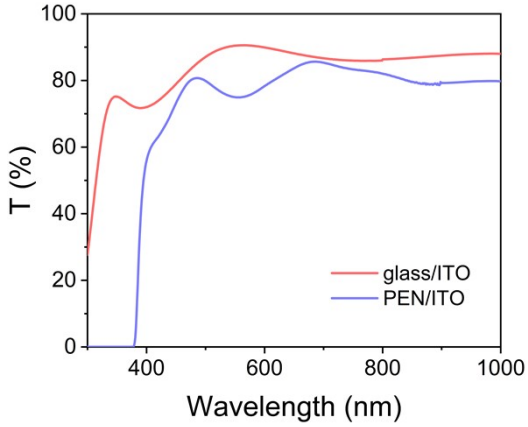

Figure S5. Transmission spectra of the glass/ITO and PEN/ITO substrates.

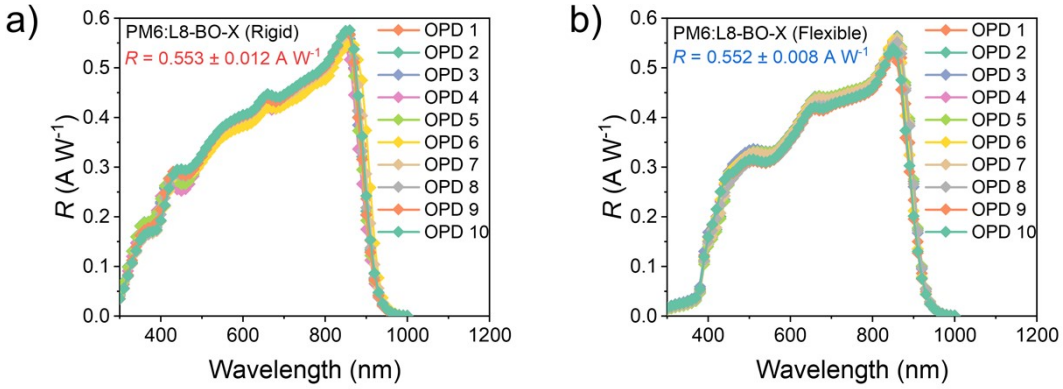

Figure S6. The responsivity curves and standard deviations of ten independently prepared rigid and flexible devices.

Table S3. Summary of reported OPDs with high responsivity.

Active layer	R_{max} (A W^{-1})	Wavelength (nm)	*Ref.*
PBDT-TT:DPPSe-4Cl:Y6	0.18	940	1
D18:FM-0F	0.24	812	2
PTB7-Th:ISC:$PC_{61}BM$	0.27	950	3
PTB7-Th:ICS	0.27	950	3
PM6:CT-Cl	0.33	950	4
PBDB-T:TBT-V-F	0.35	800	5
D18:FM-8F	0.35	970	2
PBDB-T:FM2	0.37	880	6
PTB7-Th:$PC_{70}BM$	0.37	720	7

PM6:TPCT-2F	0.39	810	8
PM7-D5:Y12	0.40	800	9
PBTTzC3:Y6	0.41	830	10
PM6:BTP-12-4F	0.42	800	11
PTB7-Th:A4T-16	0.43	750	12
PBDB-T:PZF-V:PY-IT	0.44	850	13
PM6:C5QX-B6F	0.45	800	14
PM6:BTP-eC9	0.46	820	15
PM6:PY-IT:N2200	0.47	800	16
PCE-10:BTPSV-4F:BTPSV-4Cl	0.48	870	17
PM6:WD6	0.50	800	18
PM6:Y6	0.51	830	19
PM6:CH17	0.53	830	20
PM6:L8-BO-X (Glass/ITO)	**0.55**	**850**	**this work**
PM6:L8-BO-X (PEN/ITO)	**0.55**	**850**	**this work**

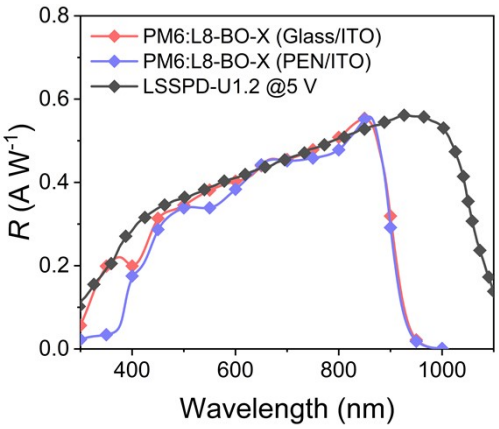

Figure S7. Comparison of response spectra between OPD and Si PD, where Si PD was purchased from commercial channels.

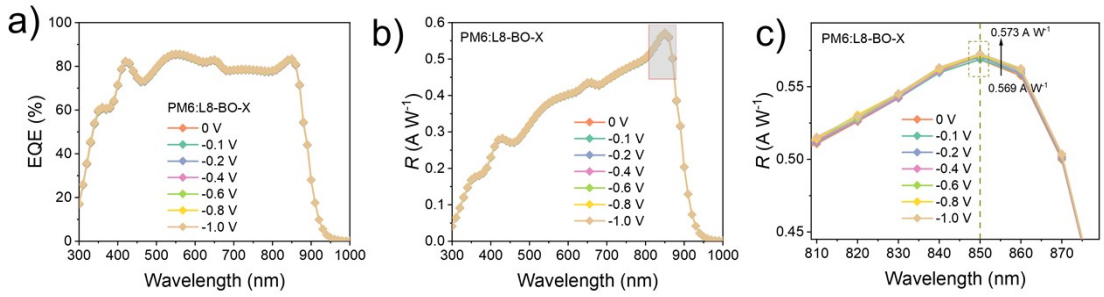

Figure S8. Bias-dependent response characteristics for a rigid OPD measured from 0 to -1 V. (a) EQE curves. (b) Responsivity curves. (c) Responsivity curves for localized enlargement.

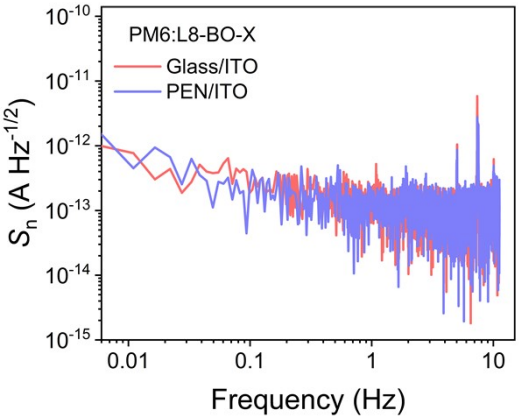

Figure S9. Noise spectral density in the dark at zero bias for OPDs.

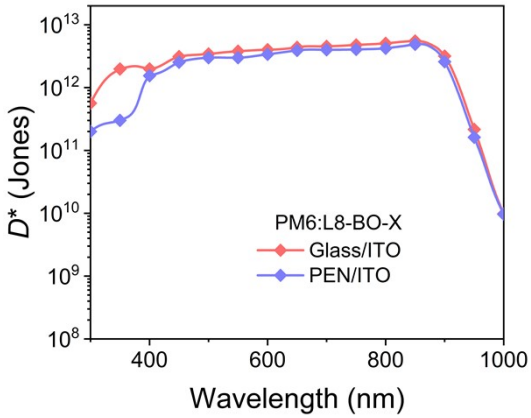

Figure S10. Specific detectivities derived from measured noises of OPDs.

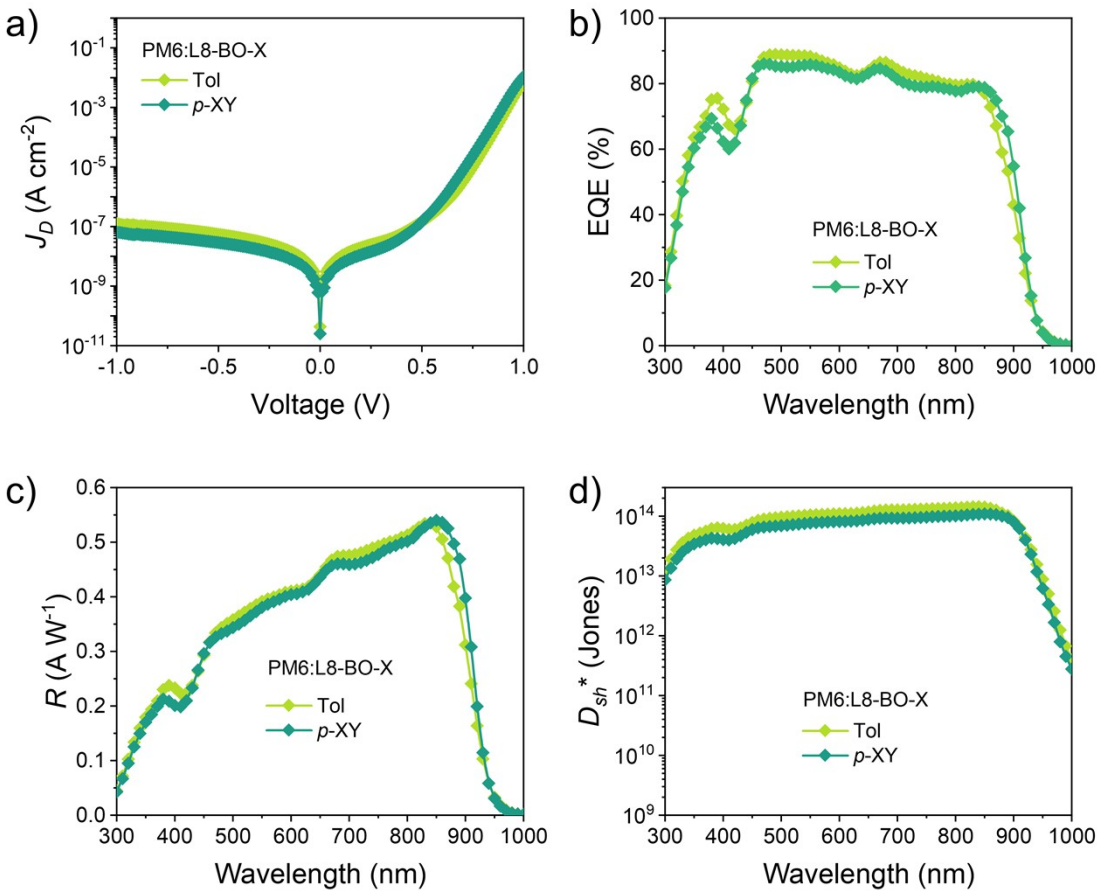

Figure S11. Performance of OPDs prepared using toluene and *p*-xylene. (a) *J*-*V* curves measured in the dark. (b) EQE curves. (c) Responsivity curves. (d) D_{sh}* curves of devices.

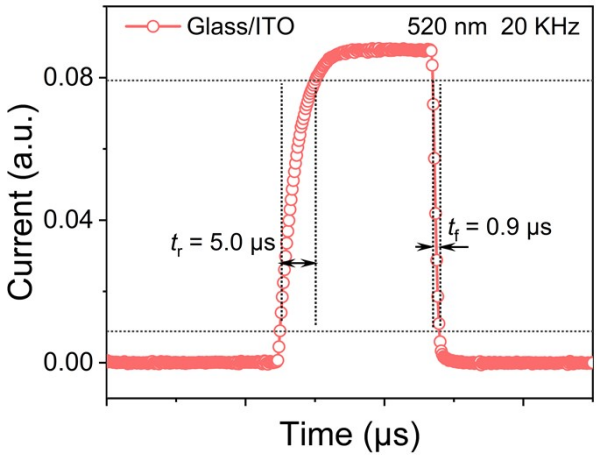

Figure S12. Response time of the rigid OPD at zero bias under 520 nm illumination.

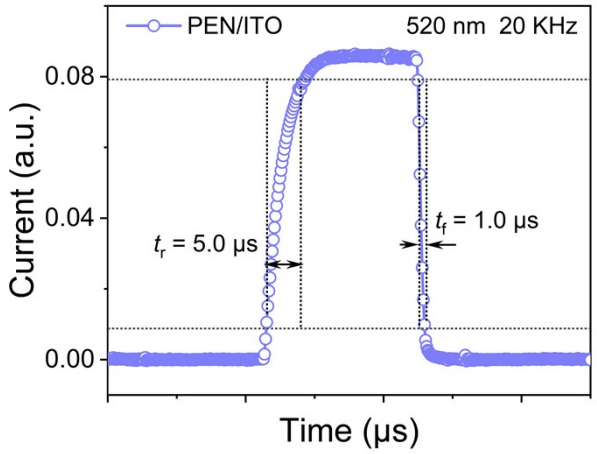

Figure S13. Response time of the flexible OPD at zero bias under 520 nm illumination.

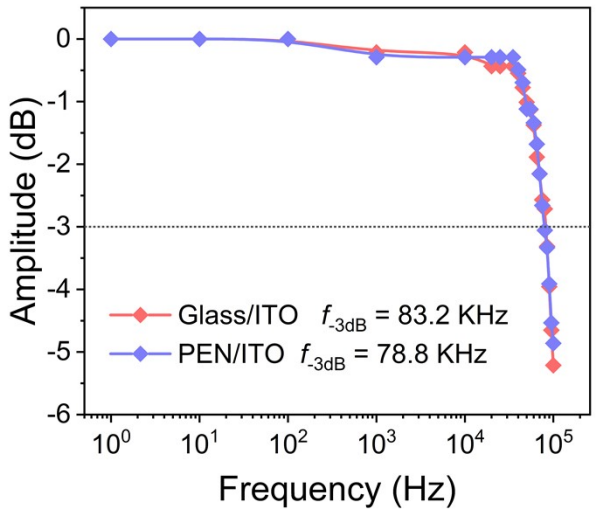

Figure S14. The -3 dB cutoff frequency of the OPDs at 520 nm.

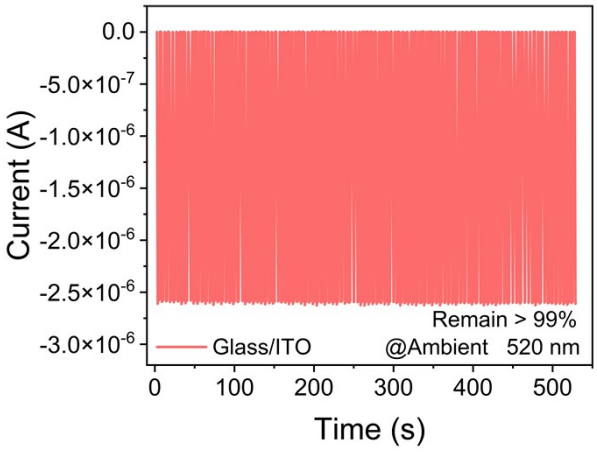

Figure S15. Cyclic stability of the rigid OPD device under ambient condition.

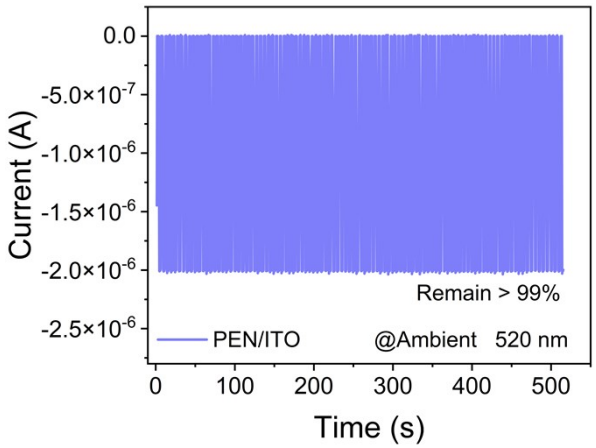

Figure S16. Cyclic stability of the flexible OPD device under ambient condition.

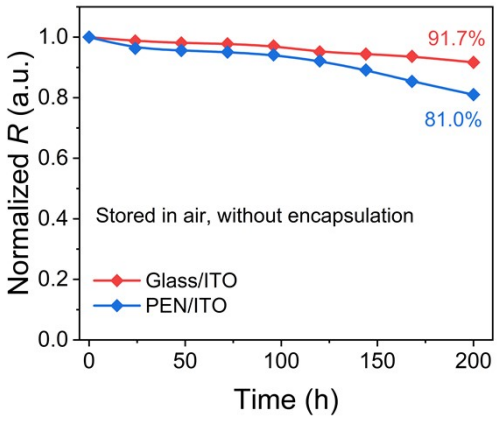

Figure S17. Normalized *R* as functions of storage time for OPDs exposing in air without encapsulation.

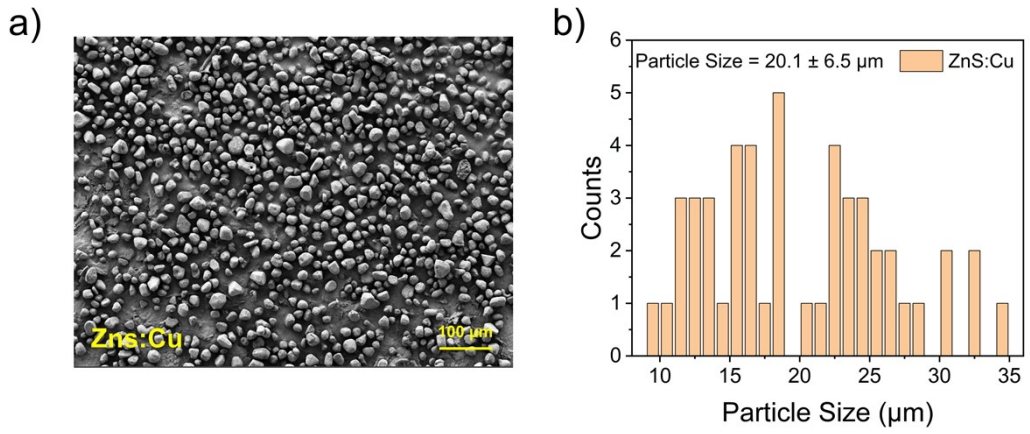

Figure S18. (a) SEM image of ZnS:Cu particles. (b) Particle size distribution of ZnS:Cu phosphor.

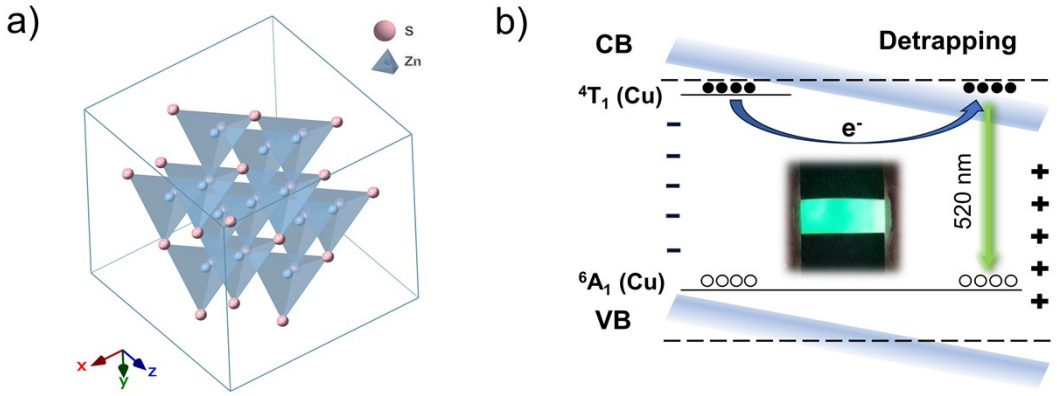

Figure S19. (a) The crystal structure of ZnS was drawn using Crystalmaker software. (b) The luminescence mechanism of ZnS:Cu, the inset illustrates a luminescence photograph of ZnS:Cu/PDMS under tensile stress.

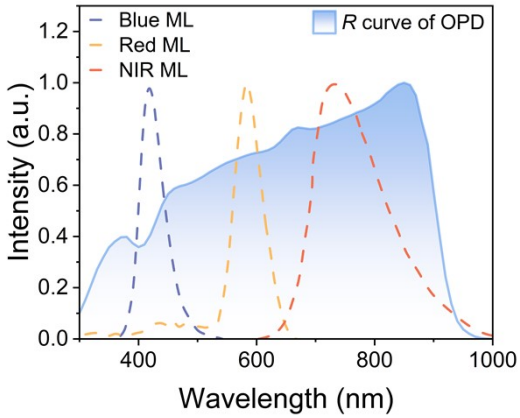

Figure S20. The normalized emission spectra of other multi-color MLs and responsivity curve of flexible OPD.

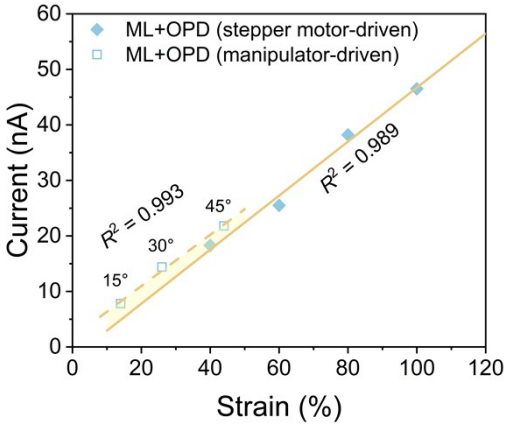

Figure S21. Output current fitting and comparison of the ML-OPD system under stepper motor drive (solid line) and manipulator drive (dash line).

Table S4. Output current of the ML-OPD system under manipulator drive.

	15°	30°	45°
Strain (%)	14	26	44
Current (nA)	7.8	14.4	21.8

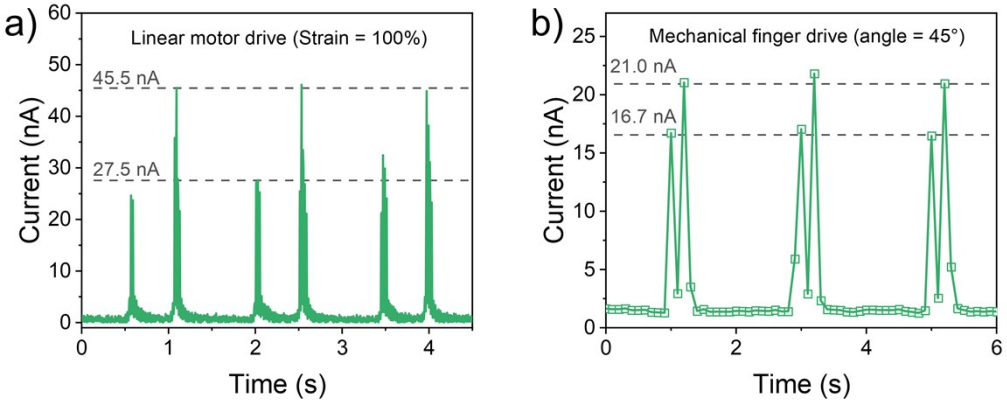

Figure S22. The current signal generated by the OPD when the ML is driven by (a) linear motor and (b) manipulator, respectively.

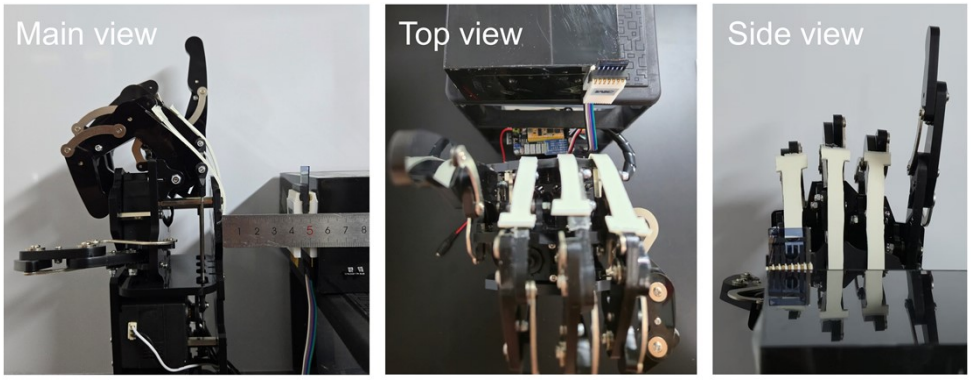

Figure S23. Photographs showing the spatial relationship between ML and OPD units in actual application demonstrations.

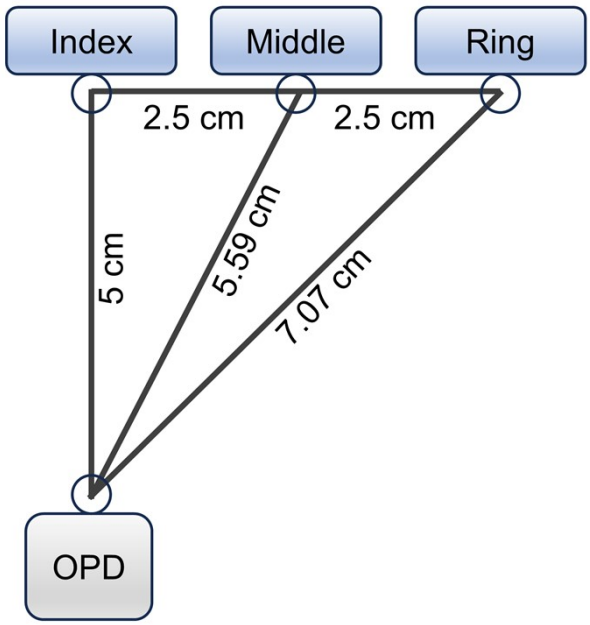

Figure S24. Schematic diagram of the spatial relationship between the ML attached to the mechanical finger and OPD units in an actual application demonstration.

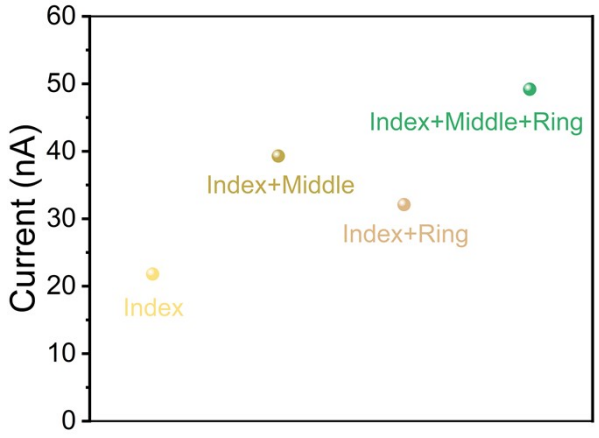

Figure S25. Current signal generated by OPD unit during multi-finger bending.

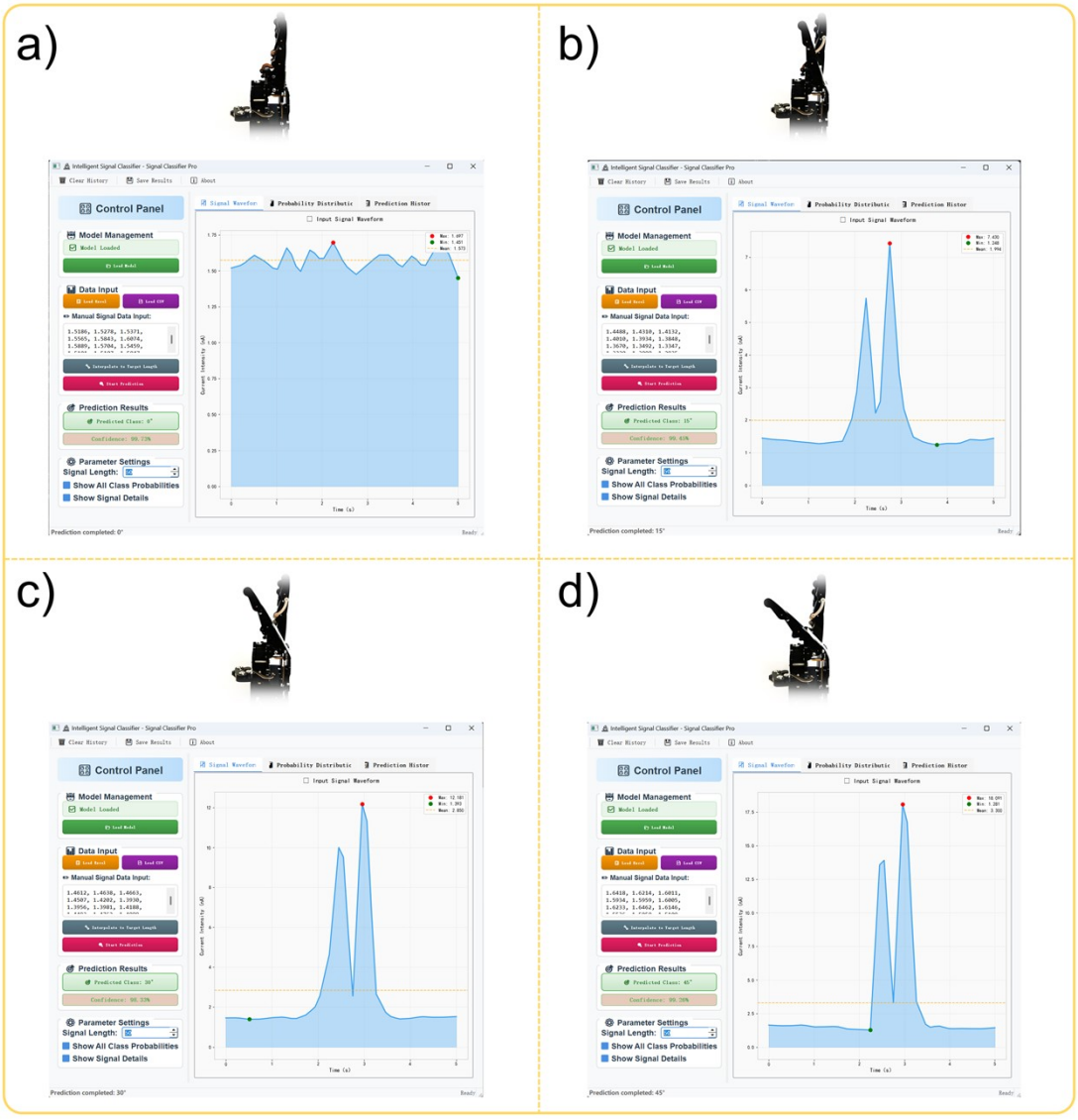

Figure S26. GUI interfaces corresponding to motion tracking signals for isolated finger bending. (a) 0°, (b) 15°, (c) 30°, and (d) 45°.

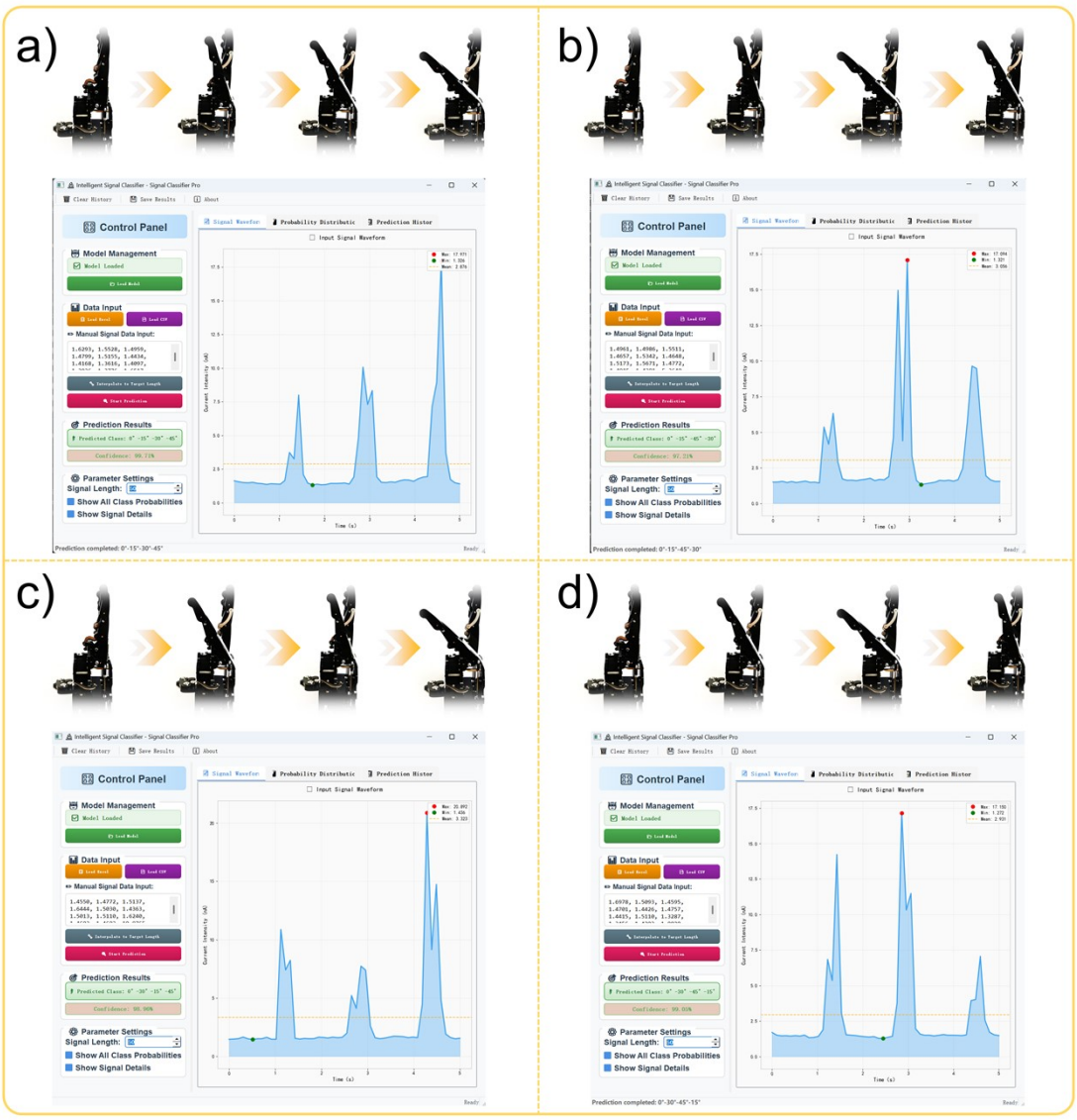

Figure S27. GUI interfaces corresponding to motion tracking signals for continuous angel bending. (a) 0°-15-30°-45°, (b) 0°-15-45°-30°, (c) 0°-30-15°-45°, and (d) 0°-30-45°-15°.

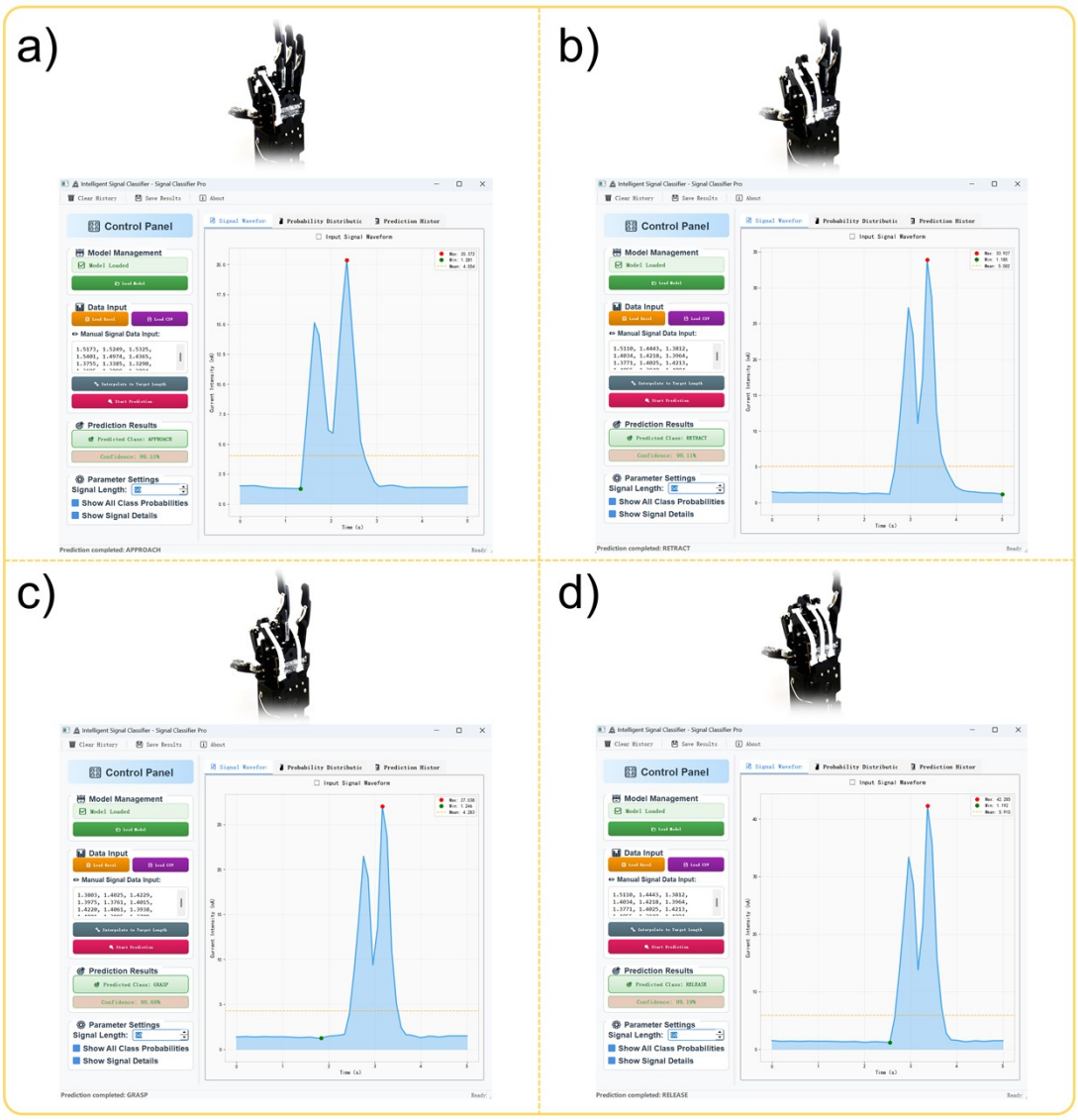

Figure S28. GUI interfaces corresponding to gesture recognition signals. (a) APPROACH, (b) RETRACT, (c) GRASP, and (d) RELEASE.

Reference

1. Y. Wang, M. Yang, B. Yin, B. Wu, G. Liu, S. Jeong, Y. Zhang, C. Yang, Z. He, F. Huang, Y. Cao and C. Duan, *ACS Appl. Mater. Interfaces*, 2024, **16**(49), 66846-66856.
2. X. Zhu, Y. Zhang, H. Li, Y. Zhang, J. Miao, J. Liu and L. Wang, *Sci. Bull.*, 2024, **69**(17), 2679-2682.
3. W. Zhong, X. Wang, W. Wang, Z. Song, Y. Tang, B. Chen, T. Yang and Y. Liang, *Adv. Sci.*, 2024, **12**(3), 2410332.
4. K. H. Huang, B. H. Jiang, H. C. Lu, Y. J. Xue, C. F. Lu, Y. Y. Chang, C. L. Huang, S. Y. Chien, C. P. Chen and Y. J. Cheng, *Adv. Sci.*, 2025, **12**(9), 2413045.
5. W. Liu, W. Guo, L. Fu, Y. Duan, G. Han, J. Gao, H. Liu, Y. Wang, Z. Ma and Y. Liu, *Angew. Chem. Int. Ed.*, 2024, **64**(4), e202416751.
6. Y. Zhang, Y. Yu, X. Liu, J. Miao, Y. Han, J. Liu and L. Wang, *Adv. Mater.*, 2023, **35**(20), 2211714.
7. Y. Lee, S. Biswas, D. H. Nam, J. W. Park, H. Jang, H. Choi, J. Kim, D. W. Park and H. Kim, *Adv. Energy Mater.*, 2025, **15**(16), 2403532.
8. H. Hou, W. Wang, T. Li, Z. Zhang, X. Miao, G. Cai, X. Lu, Y. Yi and Y. Lin, *Angew. Chem. Int. Ed.*, 2025, **64**(16), e202425420.
9. Z. Du, H. M. Luong, S. Sabury, A. L. Jones, Z. Zhu, P. Panoy, S. Chae, A. Yi, H. J. Kim, S. Xiao, V. V. Brus, G. N. Manjunatha Reddy, J. R. Reynolds and T. Q. Nguyen, *Adv. Mater.*, 2023, **36**(9), 2310478.
10. J. Park, M. I. Kim, E. D. Lee, C. Shin, H. Kim, J. Kang, H. Ahn and I. H. Jung, *Small*, 2025, **21**(21), 2410797.
11. W. Jang, H. M. Luong, M. S. Kim, T. Q. Nguyen and D. H. Wang, *Adv. Mater.*, 2024, **36**(48), 2406316.
12. N. Yang, Y. Cui, W. Fu, X. Ma, T. Zhang, W. Wang, Y. Xiao, Z. Chen, Q. Kang, G. Zuo and J. Hou, *ACS Energy Lett.*, 2025, **10**(5), 2468-2476.
13. H. T. Chandran, R. Ma, Z. Xu, J. C. Veetil, Y. Luo, T. A. Dela Peña, I. Gunasekaran, S. Mahadevan, K. Liu, Y. Xiao, H. Xia, J. Wu, M. Li, S. W. Tsang, X. Yu, W. Chen and G. Li, *Adv. Mater.*, 2024, **36**(38), 2407271.

14. Y. Yang, Y. Sun, D. Gao, C. Chen, J. Zhou, J. Cheng, L. Wang, D. Liu, W. Li and T. Wang, *Adv. Funct. Mater.*, 2025, e12335.
15. J. W. Qiao, F. Z. Cui, W. Q. Zhang, R. H. Gui, Z. Fu, M. Sun, P. Lu, H. Yin, X. Y. Du and X. T. Hao, *Adv. Mater.*, 2025, **37**(12), 2418844.
16. Y. Wang, M. Li, R. Wang, H. Shi, F. Li, Y. Zhu, G. Li, W. Ni, Y. Chen, M. Li and Y. Geng, *ACS Appl. Mater. Interfaces*, 2025, **17**, 42162-42173.
17. Y. Xia, J. Zhang, T. Guo, H. Wang, C. Geng, Y. Zhu, R. Han, Y. Yang, G. Song, X. Wan, G. Li and Y. Chen, *Adv. Funct. Mater.*, 2024, **35**(2), 2412813.
18. W. Shi, Q. Han, Y. Zhu, Y. Xia, T. He, S. Wang, L. Li, W. Ma, G. Long, G. Li, Z. Yao, C. Li, X. Wan and Y. Chen, *Natl. Sci. Rev.*, 2025, **12**(1), nwae409.
19. S. Deng, J. Wang, J. Miao, J. Ma, J. Hu and J. Liu, *Adv. Opt. Mater.*, 2025, **13**(14), 2403477.
20. Y. Zhu, H. Chen, R. Han, H. Qin, Z. Yao, H. Liu, Y. Ma, X. Wan, G. Li and Y. Chen, *Natl. Sci. Rev.*, 2024, **11**(3), nwad311.